Diffusion processes as possible mechanisms for Cr depletion at SCC crack tip

J. Nguejio, C. Guerre, F. Gaslain, C. Duhamel, J. Crepin, F. Jomard, Marc Maisonneuve

To cite this version:

J. Nguejio, C. Guerre, F. Gaslain, C. Duhamel, J. Crepin, et al.. Diffusion processes as possible mechanisms for Cr depletion at SCC crack tip. 18th International Conference on Environmental Degradation of Materials in Nuclear Power Systems - Water Reactors, Aug 2017, Portland, United States. pp.337-357, 10.1007/978-3-319-67244-1_22 . cea-02435083

HAL Id: cea-02435083

https://cea.hal.science/cea-02435083

Submitted on 26 Oct 2020

Diffusion Processes as Possible Mechanisms for Cr Depletion at SCC Crack Tip

Josiane Nguejio, Jérôme Crépin, Cécile Duhamel, Fabrice Gaslain, Catherine Guerre, François Jomard and Marc Maisonneuve

Abstract Two mechanisms are studied to explain the asymmetrical chromium depletions observed ahead of SCC crack tips in nickel-base alloys: diffusion-induced grain boundary migration (DIGM) and plasticity-enhanced diffusion. On the one hand, DIGM is evidenced in a model Alloy 600 by focused ion beam (FIB) coupled with scanning electron microscopy (SEM) cross-section imaging and analytical transmission electron microscopy (TEM) after annealing at 500 °C under vacuum and at 340 °C after exposure to primary water. The occurrence of grain boundary migration depends on the grain boundary character and misorientation. On the other hand, the effect of plasticity on chromium diffusion in nickel single-crystals is investigated by performing diffusion tests during creep tests at 500 and 350 °C. An enhancement of Cr diffusion is observed and a linear relationship between the diffusion coefficient and strain rate is evidenced. At last, in an attempt to discriminate the two mechanisms, an analytical modeling of the Cr-depleted areas observed at propagating SCC crack tips is proposed.

Keywords Diffusion · Alloy 600 · Chromium depletion · DIGM · Plasticity

---

J. Nguejio · J. Crépin · C. Duhamel (✉) · F. Gaslain
MINES ParisTech, PSL Research University, MAT-Centre des matériaux,
CNRS UMR 7633, BP 87 91003 Evry, France
e-mail: cecilie.duhamel@mines-paristech.fr

J. Nguejio · C. Guerre · M. Maisonneuve
DEN-Service de la Corrosion et du Comportement
des Matériaux dans leur Environnement (SCCME), CEA,
Université Paris-Saclay, 91191 Gif-sur-Yvette, France

F. Jomard
Laboratoire GEMaC, UMR 8635, CNRS—Université de Versailles,
45 Avenue des Etats-Unis, 78035 Versailles Cedex, France

J.H. Jackson et al. (eds.), *Proceedings of the 18th International Conference on Environmental Degradation of Materials in Nuclear Power Systems – Water Reactors*,
The Minerals, Metals & Materials Series, https://doi.org/10.1007/978-3-319-67244-1_22

Introduction

Oxidation is supposed to play a key role in the stress corrosion cracking mechanism of nickel-base alloys. Indeed, the formation of intergranular oxides at grain boundaries is supposed to be the preliminary step to crack initiation while crack propagation occurs by successive cracking of the oxide formed ahead of the crack tip [1]. In both cases, the formation of a Cr-rich oxide, sometimes identified as Cr_2O_3, is observed either at intergranular oxide or crack tips, often associated with the formation of a Cr-depleted area aside and ahead of the tip [2–8]. Detailed characterizations of crack tips performed using analytical transmission electron microscopy (ATEM) showed that leading cracks observed in the cross-section are characterized by the dissymmetric formation of Cr_2O_3 coupled with a Cr-depleted area at their tip [5]. The Cr-depleted area extends in one of the grains adjacent to the grain boundary as well as along the grain boundary itself. In addition, a Cr concentration of 10 wt% (compared to the 16 wt% of the nominal Alloy 600) can be measured [5].

Based on these observations, it was suggested that the rate-controlling step for SCC crack propagation was the Cr diffusion in the alloy. Laghoutaris et al. [5, 9] explained the dissymmetry of the Cr-depleted area as the result of a strain and strain rate heterogeneity between the two grains adjacent to the grain boundary. The grain with the most favorable orientation with respect to the mechanical loading will deform sooner and thus contain a higher density of defects (e.g. dislocations, vacancies …) that will promote a preferential oxidation and Cr depletion. However, Cr depletions are also observed in the vicinity of intergranular oxides formed in non-stressed and non-strained materials and diffusion-induced grain boundary migration (DIGM) has been reported as possible mechanism [10, 11]. DIGM is a phenomenon in which the sideways migration of grain boundaries due to diffusion of solute along them leaves in its wake an area either enriched or depleted in solute depending on solute diffusion direction [12].

The aim of this study is to evaluate (i) the effect of plastic straining on diffusion and (ii) DIGM as possible mechanisms to account for the formation of Cr-depleted areas at SCC crack tips. In a first step, the DIGM was studied in a model Alloy 600. For this purpose, thermal treatments were performed in secondary vacuum at 500 and 350 °C. Any evidence of grain boundary migration associated with a modification of the alloy composition was investigated using scanning electron microscopy (SEM) coupled with focused ion beam (FIB) and transmission electron microscopy (TEM). The formation of Cr-depleted areas was also investigated after exposure of the material to primary water. Secondly, the effect of plastic deformation on Cr diffusion in nickel was studied by carrying out diffusion tests during creep at 500 and 350 °C. At last, the results obtained in both cases were compared and their validity to explain the formation of Cr-depleted areas at SCC crack tips will be discussed.

Experimental

Materials

DIGM is studied on a model Ni–Cr–Fe alloy with a chemical composition close to that of Alloy 600 (Table 1) provided by Ecole Nationale Supérieure des Mines de Saint-Etienne (ENSME). The alloy is prepared by casting then forged and recrystallized. To facilitate the investigations, a material with millimeter-sized grains is used. Samples with a thickness of 1–2 mm are cut from the alloy and polished with SiC paper up to grade 4000 then with ¼ µm diamond paste. A final polishing is performed with colloidal silica suspension.

The effect of plasticity on Cr bulk diffusion in nickel single-crystals (purity: 99.98%) is studied using flat tensile specimens. The specimens are machined so that the surfaces have a {110} orientation and the tensile axis is along a ⟨001⟩ direction (Fig. 1).

The specimens were polished to a mirror finish using a colloidal alumina suspension. Then, a thin layer of chromium ^{52}Cr was deposited by vacuum evaporation on one of the surfaces using a Quorum K975X evaporator. Cr evaporation was performed under a secondary vacuum of 8×10^{-5} mbar with a current of 40 A up to a targeted thickness of 20 nm. The thickness of the Cr thin film was checked by atomic-force microscopy (AFM) and TEM. As Cr is very sensitive to oxidation, X-ray photoelectron spectroscopy (XPS) was carried out after Cr deposition. The $2p_{3/2}$ peaks characteristic of Cr^{0} (binding energy: 573.8 eV) and Cr^{3+} (binding energy: 576.9 eV) are observed at the surface of the thin film revealing that it is

Table 1 Chemical composition of Alloy 600 (in wt%)

Ni	Cr	Fe	C	S	O	N
Bal.	16.10	10.26	0.0062	<0.0005	<0.0010	<0.0005

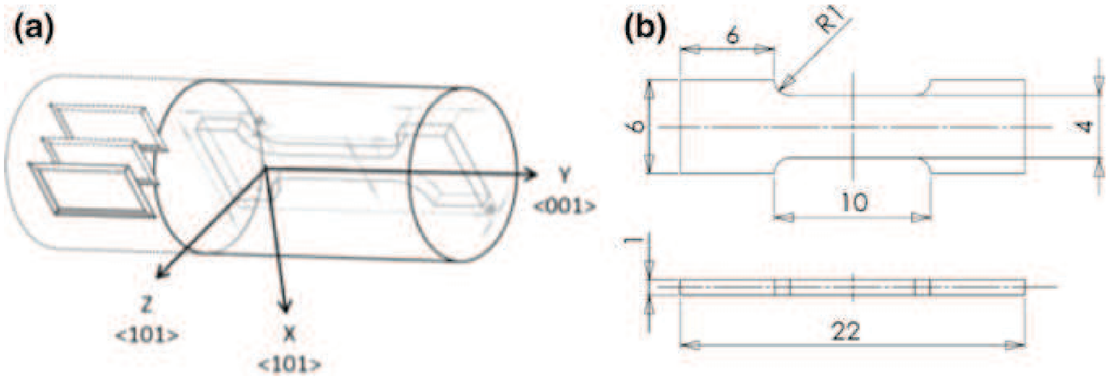

Fig. 1 **a** Scheme of the tensile specimen machining in the single crystal nickel bar, **b** geometry of the flat tensile specimens. The dimensions are given in mm

oxidized. However, after sputtering the Cr coating for 20 s and 40 s, the intensity of the Cr^{3+} $2p_{3/2}$ peak strongly decreases, showing that the remaining oxidation is superficial.

DIGM: Thermal Treatments and Microstructural Characterizations

Before the thermal treatments, the surfaces of the Ni–Cr–Fe samples are characterized by electron backscattered diffraction (EBSD) in order to map the morphology of the grains and to measure the grain boundary misorientations. The thermal treatments are performed under vacuum ($P \approx 10^{-7}$ mbar) at 360 °C for 1000 h, to approach temperature and time conditions representative of 'standard' oxidation tests in primary water, and at 500 °C for 30 h. As DIGM is thermally-activated, the phenomenon is expected to be enhanced at the latter temperature. Additionally, an oxidation test was carried out in primary water (high purity water containing 1000 ppm boron as H_3BO_3 and 2 ppm lithium as LiOH) in a stainless steel autoclave at 340 °C for 1000 h with 30 mL(STP) $kg^{-1}(H_2O)$ of dissolved hydrogen to check the formation of a Cr-depleted area associated to intergranular oxidation in the studied material.

After the tests, the specimens are characterized by coupling FIB cross sectioning and SEM imaging using a FEI Helios NanoLab 660 FIB/SEM. FIB/SEM allows site-specific characterization of the migration of grain boundaries selected from the EBSD maps (Table 2). When grain boundary migration is suspected from FIB/SEM observations, TEM thin foils are lifted out and characterized using a FEI TECNAI F20-ST field emission gun microscope equipped with an Energy Dispersive X-ray (EDX) device, a Scanning TEM (STEM) system and High-Angle Annular Dark Field (HAADF) detector as well as a Gatan Imaging Filter (GIF). Chemical elemental maps are acquired by EFTEM (Energy Filter Transmission Electron Microscopy).

Diffusion During Creep

Diffusion experiments are performed simultaneously to creep tests in vacuum ($P \approx 10^{-5}$ mbar) on single-crystal nickel tensile specimens coated with a Cr thin film. Part of the experiments is conducted at 500 °C. At this temperature, the bulk diffusion coefficient of Cr in non-stressed and non-strained Ni is expected to be high enough to be experimentally measured and to constitute a reference value. A series of tests are also performed at 350 °C as it is a characteristic temperature of SCC tests in primary water during which the Cr-depleted areas are formed.

Table 2 Investigated low-angle and high-angle grain boundaries for the DIGM study (Yes: DIGM and No: no DIGM)

Grain boundary	Misorientation (°)	500 °C—30 h Secondary vacuum	360 °C—1000 h Secondary vacuum	340 °C—1000 h Primary water
1	10	No	–	–
2	28	Yes	–	–
3[a]	37	Yes	No	–
4	37	Yes	–	–
5	28	–	No	–
6	25	–	No	Yes
7	43	–	No	Yes
8	8	–	–	No
9	25	–	–	Yes
10[a]	35	–	–	Yes
11[a]	51–60	–	–	No

[a] These grain boundaries were also observed before any thermal treatment and are used as references

For each temperature, various loads are applied. The specimen is first heated up to the test temperature. Once the temperature is stabilized, the load is applied up to the targeted value and then maintained. The load values are chosen in order to apply a stress higher than the yield stress estimated at 48 ± 2 MPa and 55 ± 5 MPa at 500 and 350 °C, respectively. Each specimen has thus undergone plastic deformation before the load maintain. The stress values applied during the creep test as well as the amount of plastic strain created during load up are reported in Table 3. According to the stress-temperature Ashby map for coarse-grained nickel [13], the power-law creep regime, characteristic of a dislocation–creep mechanism, should be reached with the chosen creep conditions. A paint speckle is deposited on the surface which is not coated with Cr to allow strain measurement by digital image correlation (DIC) during the creep tests. In order to separate the contribution of the dislocation density from that of the dislocation motion, as far as possible, all the tests were stopped at a similar final strain value close to 5–7%. The final strain corresponds to the plastic strain cumulated both during the load up and the creep stages.

After the creep tests, the diffusion profiles were acquired by secondary ion mass spectrometry (SIMS) using a CAMECA IMS-7f system. Due to its very good in-depth resolution of a few nm, SIMS allows accurate depth profiling over short diffusion distances with a low detection limit in the ppm to ppb range. SIMS analyses were performed using an O_2^+ primary ion beam with a primary ion energy of 5 keV, delivering a 20 nA current and under an O_2 pressure close to 2.10^{-6} mbar. The checkerboard technique [14] was used to deal with the surface roughness generated by the emergence of deformation bands as it allows sputtering artefacts

Table 3 Temperature (T), stress (σ) and time (t) conditions used for the creep tests. The strain after load up (ε_l) final strain (ε_f), the strain rate during primary creep ($\dot{\varepsilon}_p$) and secondary creep ($\dot{\varepsilon}_s$) as well as the measured effective diffusion coefficient D_{eff} are also given

Sample name	T (°C)	σ (MPa)	t (h)	ε_l (%)[a]	ε_f (%)[a]	$\dot{\varepsilon}_p$ (10^{-7} s^{-1})	$\dot{\varepsilon}_s$ (10^{-7} s^{-1})	D_{eff} (10^{-17} cm^2/s)
A0	500	0	146	0	0	0	0	4.0 ± 0.6
A1		55	29	0.4	5.0	5.5	3.8	5.9 ± 1.4
A2		60	29	0.6	5.3	6.0	5.6	7.7 ± 0.3
A3		65	5	1.4	3.8	45	16	32 ± 10
A4		70	3	1.3	2.6	55	19	200 ± 57
A5		74	4	3.1	7.5	64	33	420 ± 250
B0	350	0		0	0	0	0	$\approx 1.10^{-5}$[b]
B1		74	31	1.1	1.6	1.3	0.3	5.7 ± 1.8
B2		84	4	1.2	1.4	4.7	1.2	13 ± 4.7
B3		97	26	3.2	5.9	5.3	1.8	8.6 ± 6.0
B4		100	5	3.6	4.8	11	3.3	22 ± 12

[a] Corrected from the thermal strain due to thermal expansion

[b] Extrapolated from the Arrhenius law for Cr bulk diffusion in nickel

leading to non-sputtered zones in the crater to be avoided. In the checkerboard technique, ionic images are produced by raster scanning, where a primary ion beam, finely focused, scans the sample in a raster pattern. The secondary ion intensities are then saved as a function of the beam position. After the analyses, by coupling SEM images of the crater and the SIMS ionic images, it is thus possible to select areas with a uniform depth over which the concentration profiles will be extracted. It was checked that, for a uniform crater depth, the extracted diffusion profile was independent of the size of the selected area. However, for most of the analyses, a 35×35 μm^2 area was selected. The as-obtained intensity vs. sputtering time data are converted to intensity vs. depth profiles. The depth scale was calibrated by measuring at least three depth profiles per crater using a Dektak8 contact profilometer and assuming a constant sputtering rate. At least three SIMS craters were made for each diffusion conditions.

Results

Diffusion-Induced Grain Boundary Migration

As-Received State

In order to control the morphology of the grain boundaries before any thermal treatment or oxidation test, FIB/SEM imaging in backscattered electron (BSE) mode is performed on three random high-angle grain boundaries (HAGBs)

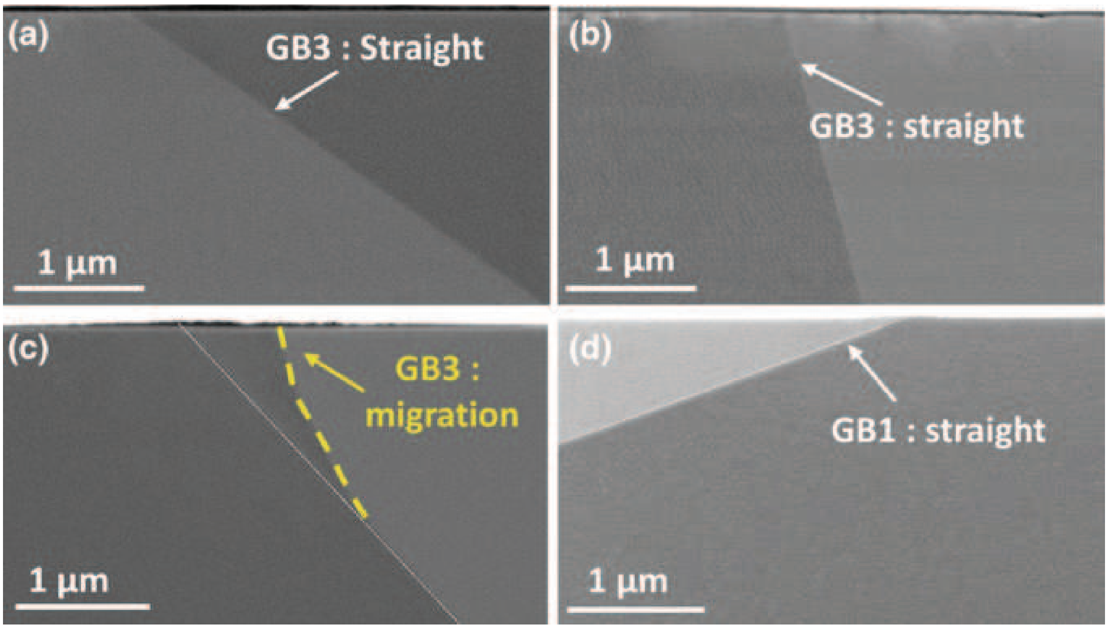

Fig. 2 SEM/FIB images in backscattered electron mode of grain boundaries (GB) observed in cross-section before and after thermal treatments in secondary vacuum; **a** GB3 before thermal treatment; **b** GB3 after 1000 h at 360 °C; **c** GB3 after 30 h at 500 °C; **d** GB1 after 30 h at 500 °C

(misorientation angles given in Table 2). All of them are perfectly straight as illustrated for GB3 in Fig. 2a.

After Annealing Under Vacuum

Four HAGBs are characterized by FIB/SEM cross-sectioning and imaging after annealing at 360 °C for 1000 h (Table 2). For all of them, no grain boundary motion is observed as illustrated in Fig. 2b for GB3. The grain boundaries remain perfectly straight and look very similar to those characterized in the as-received state. Additional TEM analyses (not shown here) performed on GB6 confirm that no evolution of the chemical composition is detected in the vicinity of the grain boundary.

After annealing at 500 °C for 30 h, a sideway motion from the straight position is observed close to the surface for the three analyzed HAGBs, suggesting that DIGM occurred in these cases. Figure 2c exemplifies this migration for GB3 where the sideway motion is indicated by a yellow dashed line. On the contrary, the characterized low-angle grain boundary (LAGB) remains perfectly straight (Fig. 2d). In addition, compared to the LAGB, significant preferential oxidation is observed at the surface of the HAGBs, above the area affected by the grain boundary migration as evidenced by the dark contrast shown in Fig. 3.

In order to check that the grain boundary motion is associated with a change in the chemical composition, TEM analyses are performed on the three HAGBs as illustrated for GB3 in Fig. 4. Similar results are found for the two other grain

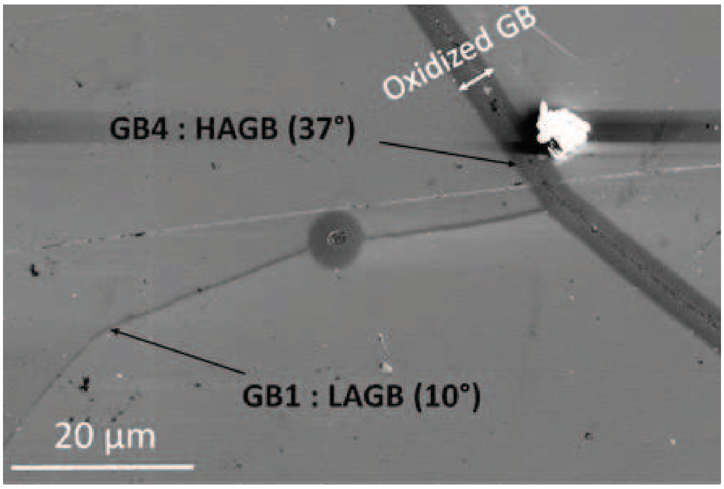

Fig. 3 SEM top view (backscattered electron mode) of a LAGB (GB1) and a HAGB (GB4) after annealing at 500 °C for 30 h. The darker contrast reveals the formation of a thicker oxide layer at the top of the HAGB

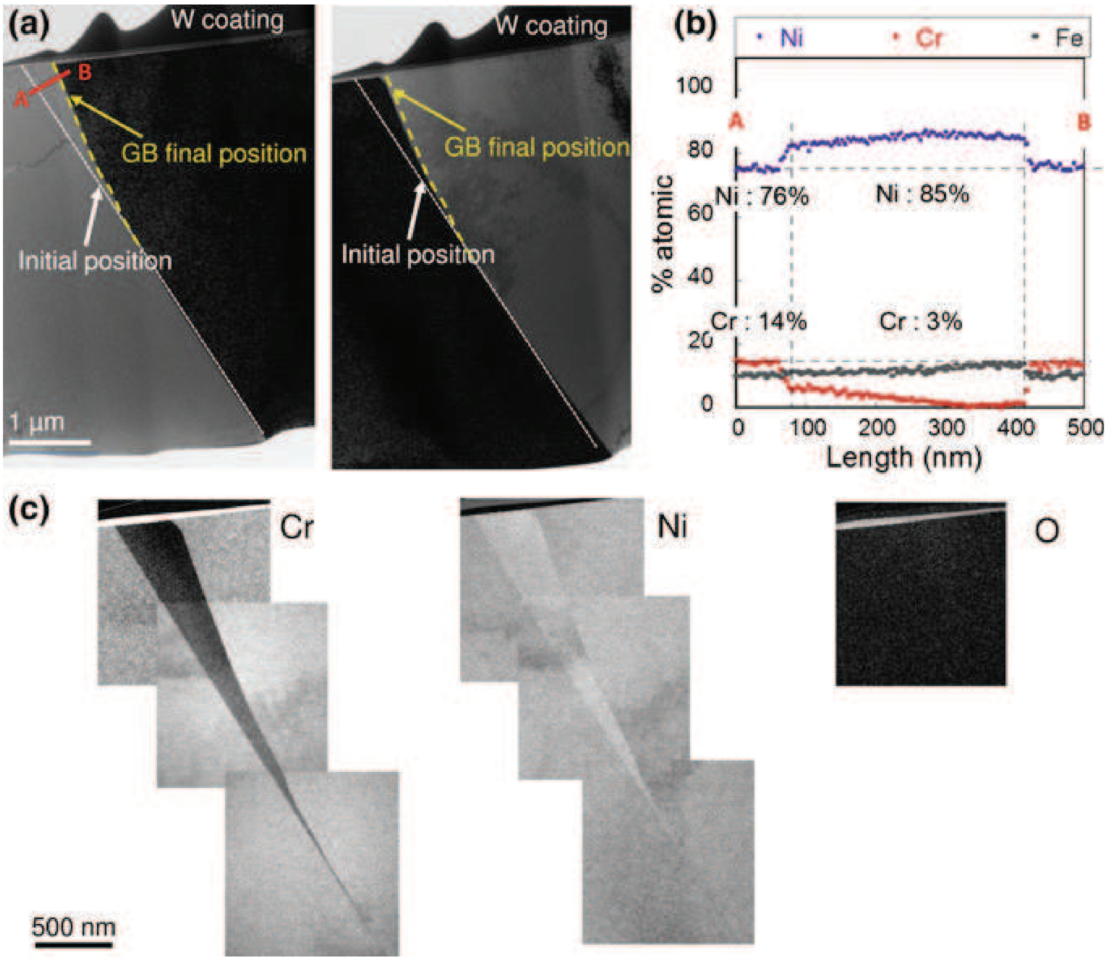

Fig. 4 TEM analyses performed on GB3 after thermal treatment at 500 °C for 30 h in secondary vacuum: **a** TEM bright field (BF) image with one of the two grains in zone axis, **b** EDX profiles acquired in STEM mode in the area affected by grain boundary migration. The position of the profile AB is indicated in the BF image, **c** EFTEM maps of Cr, Ni and O

boundaries. The grain boundary sideway motion from the straight position is confirmed by the bright-field TEM images in Fig. 4a. The images are acquired in conditions for which one of the two adjacent grains is out of contrast (zone axis ⟨311⟩ and ⟨001⟩, respectively). This evidences that the migrated area changes its crystalline orientation and adopts that of the 'growing' grain. The migrated area is measured to be 2.5 μm deep and 400 nm wide at the surface.

The evolution of the alloy composition in the migrated area is evidenced by the energy-filtered elementary maps of Cr and Ni (Fig. 4c). In these images, a brighter contrast indicates a higher amount of the analyzed element. They thus reveal that the migrated area is depleted in chromium and enriched in nickel compared to the neighboring grains. The preferential oxidation of the migrated area is also confirmed by the oxygen map that reveals the formation of a thicker oxide layer at the surface of this zone. The Cr-depleted and Ni-enriched area perfectly fits in between the actual position of the grain boundary and what is supposed to be its former position, i.e. in alignment with the grain boundary trace in the bulk. The Cr depletion is confirmed by EDX profiles acquired in STEM mode (Fig. 4b). At a given depth, the Cr content is almost constant in the width of the Cr-depleted area with steep transitions between the non-affected and affected zones (Fig. 4b). In addition, the Cr content in the depleted area increases from the surface towards the bulk as shown in Fig. 5 for GB2 and GB3. It can be seen from Fig. 5 that the depletion profiles are very similar and superimpose quite well for both grain

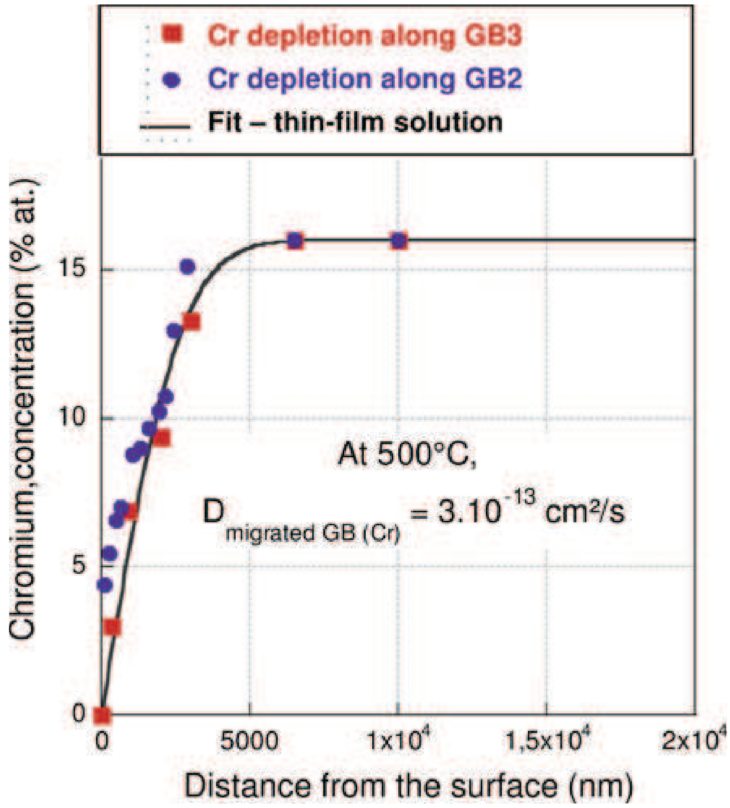

Fig. 5 In-depth Cr profiles for GB 2 and GB 3 established by STEM-EDX analyses after annealing at 500 °C for 30 h

boundaries. In addition, Cr depletion is observed ahead of the migrated area as the Cr content in the grain boundary reaches its nominal value at a depth of nearly 6 µm for both, i.e. at least twice the migration depth.

In a first approximation, the concentration constant solution of the second Fick's law (Eq. 1) is applied to estimate a diffusion coefficient of Cr in the Ni–Cr–Fe alloy at 500 °C associated with DIGM from the experimental in-depth depletion profiles obtained from the STEM-EDX analyses.

$$\frac{\mathrm{C(x,t)} - \mathrm{C_{surface}}}{\mathrm{C_{alloy}} - \mathrm{C_{surface}}} = \mathrm{erf}\left(\frac{\mathrm{x}}{2\sqrt{\mathrm{Dt}}}\right) \tag{1}$$

With x the distance from the surface, t the annealing time, C(x, t) the Cr concentration in the alloy after a time t and at a distance x, $\mathrm{C_{surface}}$ the Cr concentration at the surface ($\mathrm{C_{surface}}$ is taken equal to 0 here), $\mathrm{C_{alloy}}$ the nominal Cr concentration in the alloy and D the diffusion coefficient of Cr in the alloy.

The as-obtained diffusion coefficient is found equal to 3×10^{-13} $\mathrm{cm^2\ s^{-1}}$. This value is in agreement with the grain boundary diffusion coefficient $\mathrm{D_{gb}}$ obtained by Pruthi on a commercial Alloy 600 with a C content of 0.04 wt% ($\mathrm{D_{gb}} = 3 \times 10^{-13}$ $\mathrm{cm^2\ s^{-1}}$) [15]. It is also in agreement with the grain boundary diffusion coefficient extrapolated from Chen ($\mathrm{D_{gb}} = 4 \times 10^{-13}$ $\mathrm{cm^2\ s^{-1}}$) [16] for a model Ni–16 wt%Cr–7 wt%Fe alloy with a C content of 0.004 wt%, i.e. similar to that of our alloy (C = 0.0062 wt%).

After Oxidation in Primary Water

Six grain boundaries are characterized by FIB/SEM after oxidation in primary water including GB6 and GB7 that didn't experience DIGM after annealing at 360 °C under vacuum for 1000 h (Table 2). Intergranular oxidation is evidenced along all the selected grain boundaries (Fig. 6). For the LAGB (GB8) and for the HAGB with the highest misorientation angle (GB11), the intergranular oxidation is sharp and no deviation from what is supposed to be the initial position of the grain boundary can be detected (Fig. 6a, b). On the contrary, the other oxidized HAGBs (misorientation angle ranging between 25° and 43°) are wavy and appear to have migrated from their original position included GB6 (Fig. 6c) and GB7.

TEM analyses are performed on one grain boundary (GB6) for which no DIGM was evidenced after annealing at 360 °C under vacuum (Fig. 6). DIGM is confirmed by the EFTEM elementary maps (Fig. 6d), which clearly evidence the former position of the grain boundary as suggested by the straight interface between the Cr-depleted area and the grain on the left with the nominal composition. The migrated area is also enriched in Ni and depleted in Fe as suggested by the darker contrast observed in this region in the Fe map. The intergranular oxide, rich in Cr, seems to be formed in the wake of the moving grain boundary suggesting that oxidation occurred after grain boundary migration, in the area swept by the grain boundary motion. However, the whole area affected by the grain boundary

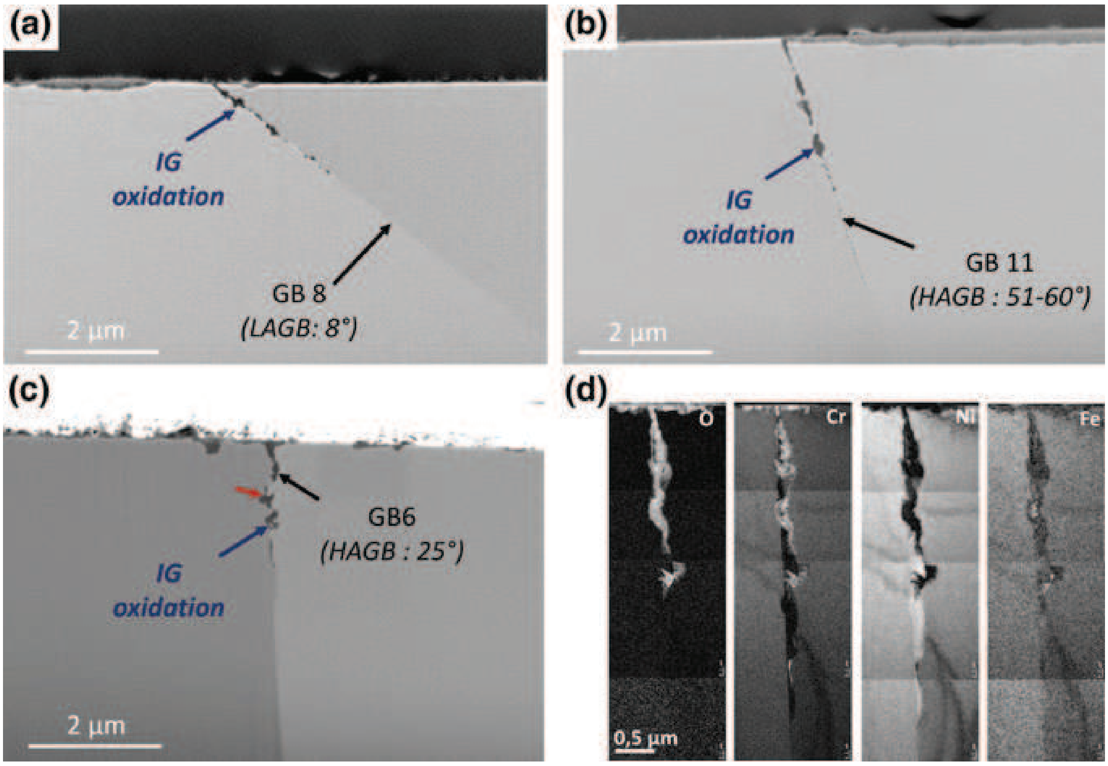

Fig. 6 FIB/SEM images in cross-section of the intergranular oxide formed after exposure to simulated primary water at 340 °C for 1000 h: **a** GB8 (LAGB), **b** GB11 (HAGB), **c** GB6 (HAGB), **d** EFTEM elemental maps of GB6 showing the intergranular oxide and the formation of a Cr-depleted area aside and ahead of the oxide

migration didn't oxidize as a Cr-depleted and Ni-enriched area is observed over a depth of 1.5 µm, ahead of the intergranular oxidation tip. The straight interface observed in Fig. 6d between the Cr-depleted area and the grain with the nominal composition suggests that DIGM occurs before intergranular oxidation as also suggested other authors [2, 10].

To summarize, DIGM is evidenced at HAGBs after annealing at 500 °C in secondary vacuum as well as after exposure to primary water at 340 °C. In both cases, it is associated with a preferential oxidation of chromium either at the surface of the alloy or along the grain boundary. On the contrary, neither DIGM nor oxidation is observed after annealing at 360 °C in secondary vacuum. The occurrence of DIGM seems thus directly linked to the outward grain boundary diffusion of chromium in the alloy to get oxidized as suggested also by the estimation of the diffusion coefficient made from the in-depth depletion profile at 500 °C.

Diffusion-Plasticity Coupling

In addition to the DIGM phenomenon, the effect of ongoing plastic deformation is also investigated to account for the formation of Cr-depleted areas at crack tips. For this purpose, diffusion tests are performed during creep. The temperature and load conditions applied during the creep tests are given in Table 3.

Creep Tests Results

An example of the stress and strain evolution with time during the creep tests is shown in Fig. 7. First, the specimen is heated up to the targeted temperature. The heating rate is monitored to avoid any temperature overshoot and the targeted temperature is reached within 20 mn. A strain increase due to thermal expansion is observed (part (1) in Fig. 7a). Once the temperature is stabilized, the load is applied up to the targeted value (part (2) in Fig. 7a) at a strain rate ranging between 1×10^{-5} and 2×10^{-4} s^{-1}. This stage lasts less than 10 min. Then, the load is maintained at a constant value (part (3) in Fig. 7a) during 3 to 31 h depending on the test conditions (Table 3). As far as possible, the creep tests are stopped at a similar total strain value ranging between 5–7% in order to separate the effect of the dislocation density (strain effect) from that of dislocation motion (strain rate effect). However, in a few cases, the test had to be stopped earlier because tertiary creep, that leads to failure, was close to be reached.

The evolution of strain, corrected from the thermal strain due to thermal expansion, with time during the "true" creep stage is detailed in Fig. 7b where ε_0 is the strain at which the creep regime starts, ε_2 is the final strain and ε_1 is the boundary strain between primary and secondary creep. During primary creep, the strain rate continuously diminishes with time down to a constant value that typifies secondary creep (or steady-state creep). During secondary creep, the strain varies linearly with time and the strain (or steady-state creep) rate is at its lowest value, resulting from a balance between dislocation creation and annihilation. For all the

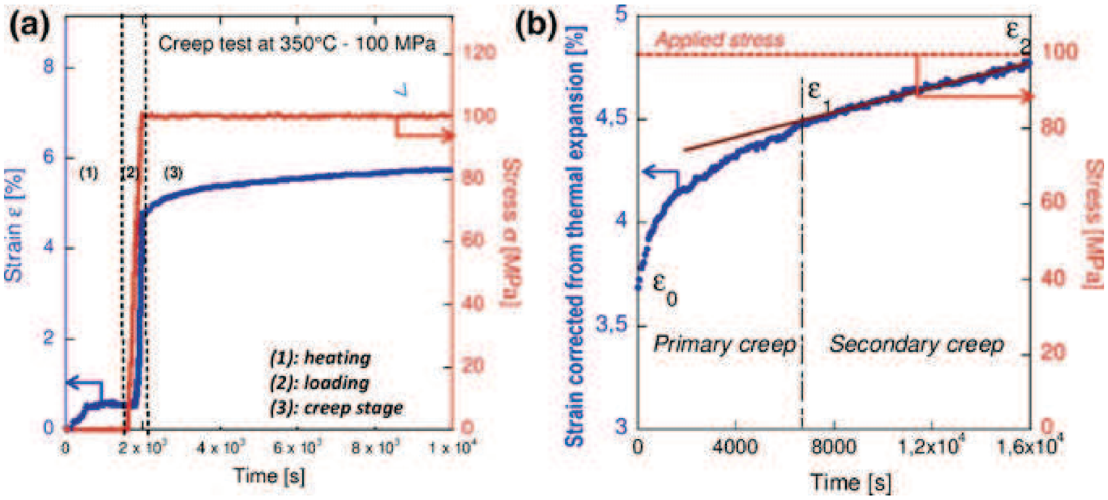

Fig. 7 **a** Example of strain-time and stress curves (vacuum, temperature: 350 °C, σ = 100 MPa), **b** zoom on the 'true' creep regime showing primary and secondary creep. The strain is corrected from the thermal expansion

tests, the mean strain rate during primary creep $\dot{\varepsilon}_p$ is estimated using Eq. 2 and reported in Table 3:

$$\dot{\varepsilon}_p = \frac{\varepsilon_1 - \varepsilon_0}{\Delta t_p} \tag{2}$$

with Δt_p the duration of primary creep.

The strain rate during secondary creep $\dot{\varepsilon}_s$ is calculated from the slope of the strain-time curve (Table 3). As expected, the mean primary creep rate is always higher than the steady-state creep rate although within the same range of order. In addition, the values for $\dot{\varepsilon}_s$ are slightly lower at 350 °C (3×10^{-8}–3.3×10^{-7} s^{-1}) than at 500 °C (3.8×10^{-7}–3.3×10^{-6} s^{-1}) and, at a given temperature, increase with stress.

Effect of Ongoing Plasticity on the Diffusion Coefficients

The diffusion profiles of Cr in the Ni specimens are acquired by SIMS analyses using the checkerboard technique described previously. In addition to the creep specimens, a diffusion profile is also acquired on a non-stressed Ni single-crystal for which a diffusion treatment was performed at 500 °C for 146 h (Fig. 8a). An example of the diffusion profiles obtained after the creep tests is given in Fig. 8c.

The thin-film solution of the second Fick's law is used to fit the experimental profile [17]:

$$C(x,t) = \frac{Q}{\sqrt{\pi D t}} \exp\left(\frac{-x^2}{4Dt}\right) \tag{3}$$

with C(x, t) the Cr concentration, Q the number of diffusing particles per unit area, D the diffusion coefficient.

The diffusion coefficient is given by the slope of the lnC-x^2 curve as given by Eq. 4.

$$\frac{\partial \ln C}{\partial x^2} = -\frac{1}{4D\,t} \tag{4}$$

The linear dependency of lnC with x^2 evidenced in Fig. 8b for the non-stressed specimen and illustrated in Fig. 8d for the stressed specimens confirming the validity of the thin-film solution for the diffusion conditions used in this study. For the stressed specimens, the diffusion coefficient is calculated considering a diffusion time equal to the total duration of the creep test, i.e. from specimen loading [start of stage (2)] to unloading [end of stage (3)]. In addition, using Eq. 4, an effective diffusion coefficient, that gathers the contributions of both the dislocation-free crystal and from the dislocations, is obtained in these cases.

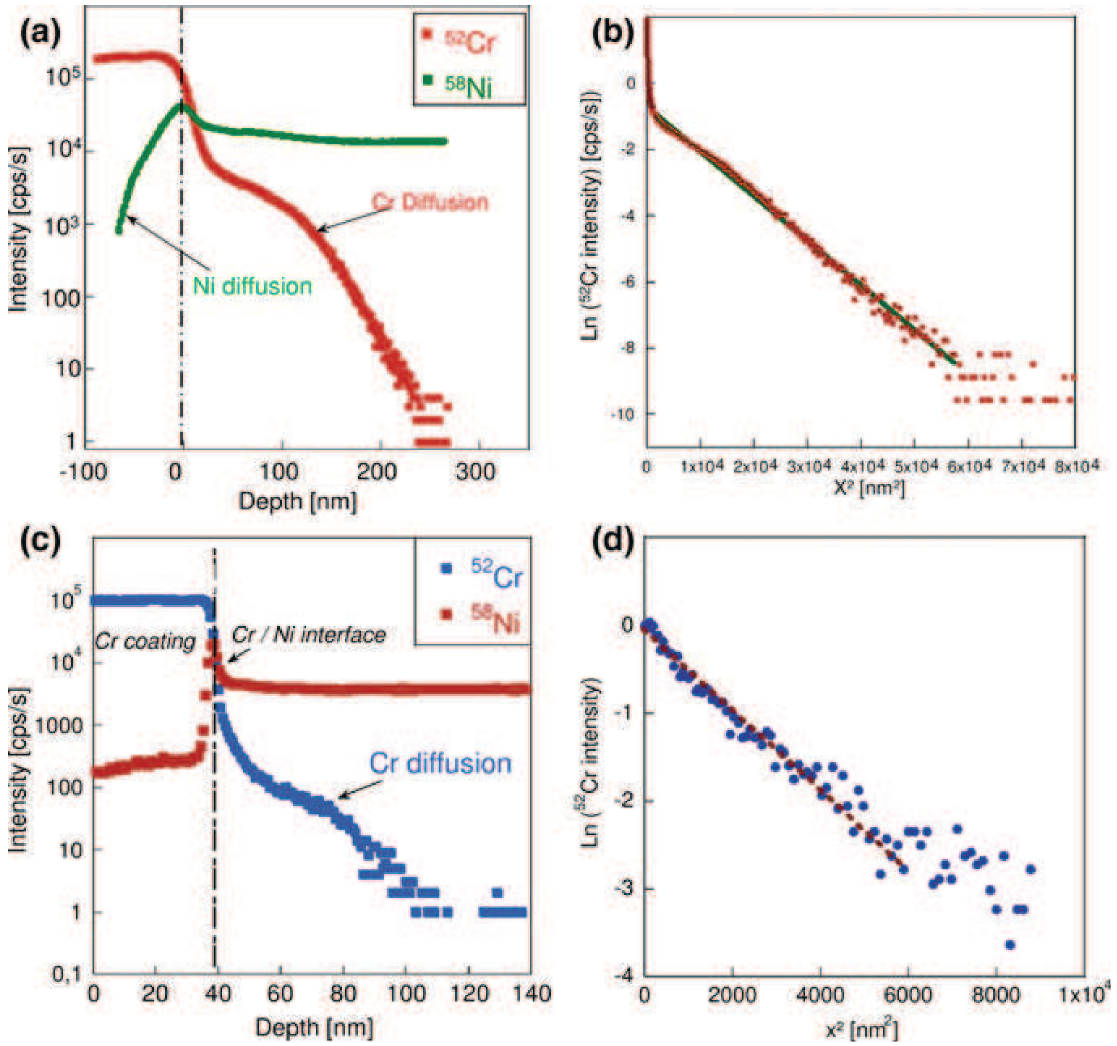

Fig. 8 **a** Chromium diffusion profile obtained on non-stressed Ni at 500 °C in vacuum and **b** linear dependency of lnC with x, **c** chromium diffusion profile obtained after a creep test in vacuum at 360 °C (σ = 100 MPa) and **d** linear dependency of lnC with x

The as-measured diffusion coefficients are reported in Table 3 for all the tested specimens. At 500 °C, without any applied stress, the bulk diffusion coefficient D_b of Cr in Ni is found equal to $(4.0 \pm 0.6) \times 10^{-17}$ cm^2 s^{-1}. For the stressed specimens, the effective diffusion coefficient is systematically higher than for the non-stressed sample and increases with the applied load and thus with the steady-state creep rate. A one-fold increase of the creep rate induces a two-fold increase of the diffusion coefficient. A similar strain rate dependency is observed at 350 °C even though, at this temperature, a one-fold strain-rate increase generates ‘only’ a one-fold increase of the diffusion coefficient. Interestingly, the diffusion coefficients measured for specimens A1 and B4, for which the steady-state creep rate is close, stand within the same range of order, suggesting that the strain rate effect is higher than thermal activation.

In an attempt to quantify this enhancement, the effective diffusion coefficient D_{eff} measured on the stressed specimens is normalized by the bulk diffusion coefficient

D_b obtained on non-stressed nickel. As shown previously, D_b was measured at 500 °C while Cr bulk diffusion is too slow at 350 °C to be experimentally measured. Therefore, the D_b value was extrapolated from literature data obtained at high temperatures, between 950 and 1300 °C [18, 19]. A value close to 10^{-22} cm^2 s^{-1} is found at 350 °C. However, this value might be under-estimated as the same extrapolation made at 500 °C gives a D_b value close to 10^{-19} cm^2 s^{-1}, i.e. two orders of magnitude lower than the one measured in this work.

The strain-rate dependency of D_{eff}/D_b is reported in Fig. 9 for both temperatures. First, a linear relationship is evidenced between D_{eff}/D_b and the strain-rate during secondary creep for both temperatures but with a temperature-dependent slope. More interestingly, the enhancement due to plastic straining is much higher at 350 °C than at 500 °C. With the bulk diffusion coefficient used as reference, at least a 5-fold increase is found at 350 °C while only a 2-fold increase is obtained at 500 °C. The trends obtained in this work are in good agreement with results on plasticity enhancement reported in the literature many years ago for other systems [20, 21] and with the model developed by Cohen and al. [20] given by Eqs. 5 and 6:

$$\frac{D_{eff}}{D_b} = 1 + B(T)\dot{\varepsilon} \tag{5}$$

$$B(T) = \frac{D_d}{D_v}\left(\frac{S}{b \cdot V_d}\right) \tag{6}$$

With D_d the diffusion coefficient along dislocations, S the total section of diffusion short-circuits, b the Burger vector and V_d the dislocation velocity.

Fig. 9 Evolution of D_{eff}/D_b with the secondary creep strain rate at 360 and 500 °C (creep tests performed in vacuum)

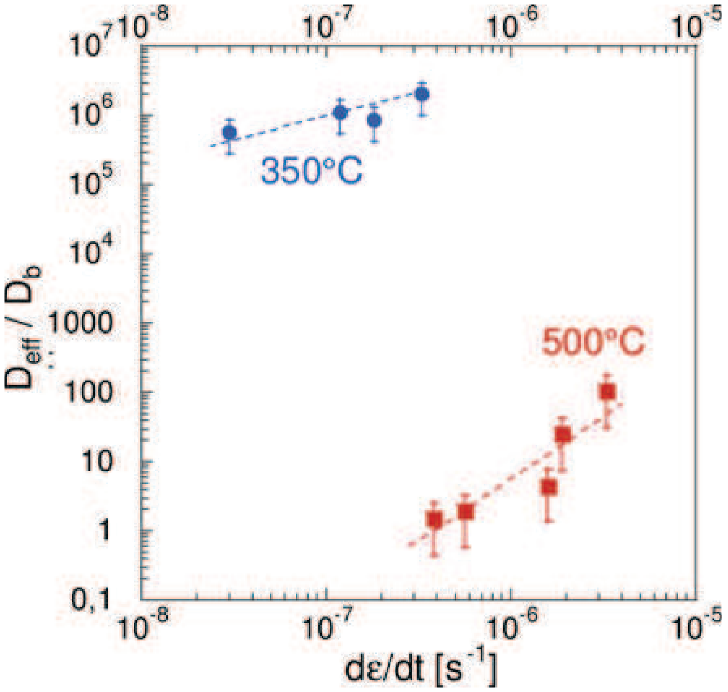

B(T) is a function of the temperature through the D_d/D_b ratio and the dislocation velocity and is constant at a given temperature. In their model, Cohen et al. assume that the dislocation velocity is constant at a given temperature. According to the Orowan relation [22], this suggests that diffusion is directly linked to the density of mobile dislocations. The higher it is, the faster diffusion is.

Modeling the Cr Depletion

The aim of this work is to identify a mechanism that could account for the Cr-depleted areas observed at the tip of SCC cracks formed during exposure to primary water at temperatures close to 350 °C. Indeed, former investigations [5] have shown that propagating cracks exhibit a specific configuration at their tips with a dissymmetric oxide Cr_2O_3 associated with a Cr-depleted area which is 20 nm-thick in the grain and 200 nm long in the grain boundary, ahead of the crack tip (Fig. 10a). In these investigations, a Cr content of 8 wt% is reported at the oxide/alloy interface. A discontinuous propagation mechanism was proposed with a propagation step equal to 200 nm. The oxide is formed in between two propagation

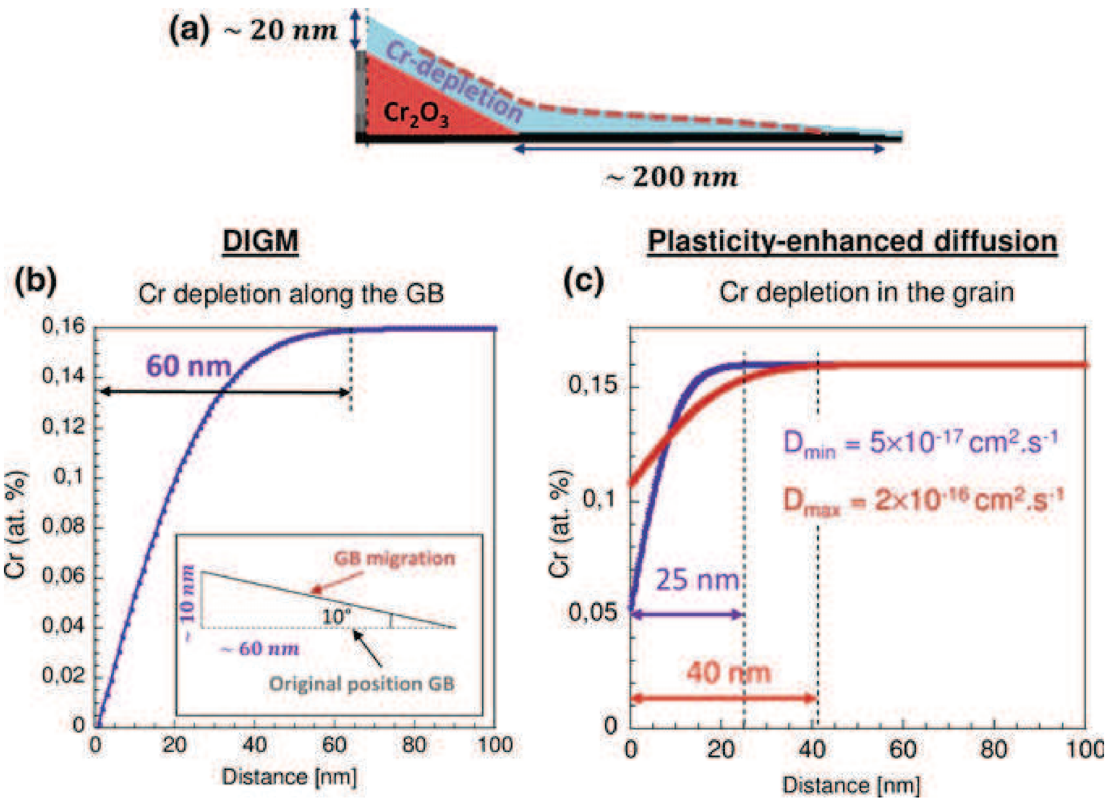

Fig. 10 **a** Schematic representation of a propagating crack tip from [5], Cr depletion profile modelled at 360 °C for an oxidation time of 6300 s, assuming **b** a DIGM mechanism, **c** a plasticity-enhanced diffusion mechanism

steps. Based on the measured initiation time, a crack growth rate of 1 mm/y is considered, leading to an oxidation time of 6300 s.

In the following, an attempt is made to model the Cr-depleted area observed at propagating SCC crack tip using the results previously exposed for the two mechanisms studied in this paper: DIGM and plasticity-enhanced diffusion. For this purpose, and in a first approximation, the analytical model developed by Wagner [23] to describe the depletion profile observed in the case the selective oxidation of a binary alloy at high temperature was used.

Description of the Wagner's Model and Used Hypothesis

The Wagner's analytical model was developed in the framework of the high temperature oxidation of binary alloys in which one chemical element is selectively oxidized. The oxidation kinetic is supposed to follow a parabolic law characterized by a parabolic kinetic constant k_p. The Wagner's model gives the complete depletion profile of the oxidized element in the alloy (Eq. 7). In this study, this model is applied to describe the selective oxidation of Cr at the tip of a Ni–Cr–Fe alloy.

$$C\ (x,t) = C_i + (C_0 - C_i) \times \left(\frac{\operatorname{erf}\left(\frac{x}{2\sqrt{\tilde{D} \times t}}\right) - \operatorname{erf}\left(\sqrt{\frac{k_c}{2\tilde{D}}}\right)}{\operatorname{erfc}\left(\sqrt{\frac{k_c}{2\tilde{D}}}\right)} \right) \tag{7}$$

with C_i the Cr concentration at the oxide/alloy interface, C_0 the Cr concentration in the bulk, $\tilde{D}$ the interdiffusion coefficient, k_c the corrosion constant.

The concentration at the oxide/alloy interface is given by Eq. 8:

$$C_i = \frac{F(u) - C_0}{F(u) - 1} \tag{8}$$

with

$$F(u) = \sqrt{\pi u^2} \cdot (1 - \operatorname{erf} u) \cdot \exp(u^2) \tag{9}$$

And

$$u = \sqrt{\frac{k_c}{\tilde{D}}}. \tag{10}$$

The corrosion constant k_c is related to the kinetic constant k_p through the Pilling and Bedworth ratio (PBR) considering Eq. 11:

$$k_c = \frac{k_p}{PBR^2} \tag{11}$$

For the Cr_2O_3/Alloy 600 couple, PBR is equal to 2.2. The kinetic constant k_p is estimated by fitting the kinetics data reported by Lefaix-Jeuland et al. [24] for an Alloy 600 exposed to primary water at 325 °C. It is assumed that the evolution of the k_p value between 325 and 350 °C is negligible. It is thus taken equal to 2×10^{-18} cm^2 s^{-1}, giving a k_c value of 4×10^{-19} cm^2 s^{-1}.

At last, in a first approximation, the interdiffusion coefficient $\tilde{D}$ is supposed equal to a diffusion coefficient of Cr in Ni.

Application to the DIGM Mechanism

In order to estimate how the Cr-depleted area would extend at the crack tip in case of a DIGM mechanism, the Wagner's model is applied at 350 °C for an oxidation time of 6300 s. To account for the fact that DIGM affects only the grain boundary regions, the grain boundary diffusion coefficient D_{GB} of Cr in Ni is used in the model. The D_{GB} value is estimated at 350 °C from the D_{GB} value found at 500 °C using an activation energy of 200 kJ mol^{-1}. This value is an average between the activation energy reported by Pruthi [15] and Chen [16], respectively, for the grain boundary diffusion of Cr in Alloy 600. The as-obtained D_{GB} value at 350 °C is 3×10^{-18} cm^2 s^{-1}. The Cr concentration profile along the grain boundary obtained using the Wagner model is shown in Fig. 10b. A Cr depletion over 60 nm along the grain boundary is obtained. The 10 nm extend of the Cr depletion in the grain is estimated using simple geometry by considering that the migrated area has a triangular shape homothetic to that observed at 500 °C (Fig. 4). At last, the DIGM mechanism allows to account for the dissymmetry of the Cr depletion at crack tip as the evolution of the chemical composition occurs in the wake of the grain boundary migration.

Application to the Plasticity-Enhanced Diffusion Mechanism

The results from Section "Diffusion-Plasticity Coupling" have shown that plasticity strongly enhances the bulk Cr diffusion in Ni. The diffusion coefficients measured at 350 °C were obtained for strain rates ranging between 3×10^{-8} and 3×10^{-7} s^{-1}. To check the validity of such measurement for SCC applications, the strain rate at the crack tip is estimated from the supposed crack growth rate using the correlation established by Le Hong et al. [25]. For a CGR of 1 mm/yr, a strain rate of 10^{-7} s^{-1} is found.

The Wagner's model is then applied using the minimum and maximum effective diffusion coefficients measured at 350 °C (Fig. 10c). The as-obtained depletion profiles show that the depleted area extends over 25–40 nm which is in agreement with the experimental observations. The dissymmetry can be explained by the dissymmetry of the plastic zone at the crack tip. If the propensity of the two adjacent grains for plastic deformation is different, the plastic zone may be dissymmetric and thus explain the dissymmetry of the Cr-depleted area. This area should be formed in the grain exhibiting the higher plastic deformation and thus the higher strain rate. However, the model doesn't account for the Cr depletion along the grain boundary ahead of the crack tip. As for the DIGM mechanism, the extent of the depletion can be estimated from the grain boundary diffusion coefficient and thus should be observed over 60 nm.

Conclusions

The aim of this work was to evaluate either DIGM or plasticity-enhanced diffusion as possible mechanisms for the formation of Cr-depleted areas at leading crack tips.

DIGM was evidenced in a model Alloy 600 for HAGBs after annealing under secondary vacuum at 500 °C and exposure to primary water at 360 °C. The occurrence of DIGM correlates with either surface or intergranular selective oxidation of chromium that acts as a driving force for intergranular chromium diffusion. The outward diffusion of Cr leads to the grain boundary migration that leaves in its wake a Cr-depleted and Ni-enriched area.

Acceleration of Cr diffusion in Ni single-crystals experiencing plastic deformation during creep test was shown. A linear dependency is found between the measured effective diffusion coefficients and the strain rate during secondary creep. Diffusion is all the more enhanced by plasticity than temperature is low, suggesting a predominant effect of plastic deformation over thermal activation.

Both DIGM and plasticity-enhanced diffusion mechanisms allow the dissymmetry of the Cr-depleted area to be described. In addition, modeling of the Cr-depleted areas observed at crack tips were performed for both mechanisms using the analytical Wagner's model and using the results obtained in this work as input data. In both cases, the modeled extent of the Cr-depleted area is in agreement with the experimental observations allowing none of the two mechanisms to be excluded at this stage. As both mechanisms may occur, further work would be necessary to evaluate the effect of plasticity on the DIGM.

Acknowledgements EDF is gratefully acknowledged for financial support. The authors want to thank SERMA Technologies (Grenoble, France) for FIB lamellae preparation for TEM observations. This work was carried out within the MATMECA consortium and supported by the ANR under contract number ANR-10-EQUIPEX-37. It has benefited from the facilities of the Laboratory MSSMat (UMR CNRS 8579), CentraleSupélec, France.

References

1. P. Scott, M. Le Calvar, Some possible mechanisms of intergranular stress corrosion cracking of Alloy 600 in PWR primary water, in *6th International Symposium on Environmental Degradation of Materials in Nuclear Power systems—Water Reactors*, 1993
2. D.K. Schreiber, M.J. Olszta, S.M. Bruemmer, Grain boundary depletion and migration during selective oxidation of Cr in a Ni–5Cr binary alloy exposed to high-temperature hydrogenated water. Scr. Mater. **89**, 41–44 (2014)
3. Y.S. Lim, S.W. Kim, S.S. Hwang, H.P. Kim, C. Jang, Intergranular oxidation of Ni-based Alloy 600 in a simulated PWR primary water environment. Corros. Sci. **108**, 125–133 (2016)
4. L.E. Thomas, S.M. Bruemmer, High-resolution characterization of intergranular attack and stress corrosion cracking of Alloy 600 in high-temperature primary water. Corrosion **56**, 572–587 (2000)
5. M. Sennour, P. Laghoutaris, C. Guerre, R. Molins, Advanced TEM characterization of stress corrosion cracking of Alloy 600 in pressurized water reactor primary water environment. J. Nucl. Mater. **393**, 254–266 (2009)
6. D.K. Schreiber, M.J. Olszta, D.W. Saxey, K. Kruska, K.L. Moore, S. Lozano-Perez, S.M. Bruemmer, Examinations of oxidation and sulfidation of grain boundaries in Alloy 600 exposed to simulated pressurized water reactor primary water. Microsc. Microanal. **19**, 676–687 (2013)
7. K. Kruska, P. Chou, O. Calonne, L. Fournier, S. Lozano-Perez, Atom-probe tomography of surface and grain boundary oxides in Alloy 600 and Alloy 690 exposed to simulated PWR primary water, in *16th International Conference on the Environmental Degradation of Materials in Nuclear Power Systems*, Asheville, US, 2013
8. M.J. Olszta, D.K. Schreiber, L.E. Thomas, S.M. Bruemmer, Penetrative internal oxidation from Alloy 690 surfaces and stress corrosion crack walls during exposure to PWR primary water, in *15th International Conference on the Environmental Degradation of Materials in Nuclear Power Systems*, 2011
9. C. Guerre, P. Laghoutaris, J. Chêne, L. Marchetti, R. Molins, C. Duhamel, M. Sennou, Stress corrosion cracking of Alloy 600 in PWR primary water: influence of chromium, hydrogen and oxygen diffusion, in *15th International Conference on the Environmental Degradation of Materials in Nuclear Power Systems*, Colorado Springs (USA), 2011
10. G. Bertali, F. Scenini, M.G. Burke, Advanced microstructural characterization of the intergranular oxidation of Alloy 600. Corros. Sci. **100**, 474–483 (2015)
11. G. Bertali, F. Scenini, M.G. Burke, The intergranular oxidation susceptibility of thermally–treated Alloy 600. Corros. Sci. **114**, 112–122 (2017)
12. A.H. King, Diffusion induced grain boundary migration. Int. Mater. Rev. **32**, 173–189 (1987)
13. H.J. Frost, M.F. Ashby, *Deformation-Mechanism Maps* (Pergamon Press, UK, 1982)
14. S.M. Daiser, C. Scholze, J.L. Maul, The checkerboard technique: an essential progress in SIMS data acquisition and evaluation. Nucl. Instrum. Methods Phys. Res. Sect. B Beam Interact. Mater. At. **35**, 544–549 (1988)
15. D.D. Pruthi, M.S. Anand, R.P. Agarwala, Diffusion of chromium in Inconel 600. J. Nucl. Mater. **64**, 206–210 (1977)
16. T.-F. Chen, G.P. Tiwari, Y. Iijima, K. Yamauchi, Volume and grain boundary diffusion of chromium in Ni-base Ni–Cr–Fe alloys. Mater. Trans. **44**, 40–46 (2003)
17. H. Mehrer, *Diffusion in Solids* (Springer, Berlin, 2007)
18. J. Růžičková, B. Million, Self-diffusion of the components in the FCC phase of binary solid solutions of the Fe–Ni–Cr system. Mater. Sci. Eng. **50**, 59–64 (1981)
19. K. Monma, H. Suto, H. Oikawa, Diffusion of Ni63 and Cr51 in nickel-chromium alloys. J. Jpn. Inst. Met. **28**, 188–192 (1964)
20. M. Cohen, Self-diffusion during plastic deformation. Trans. Jpn. Inst. Met. **11**, 145–151 (1970)

21. A.R. Wazzan, E. Dorn, Analysis of enhanced diffusivity in nickel. J. Appl. Phys. **36**, 222–228 (1965)
22. E. Orowan, Problems of plastic glide. Proc. Phys. Soc. **52**, 8–22 (1940)
23. C. Wagner, Theoretical analysis of the diffusion processes determining the oxidation rate of alloys. J. Electrochem. Soc. **99**, 369–380 (1952)
24. H. Lefaix-Jeuland, L. Marchetti, S. Perrin, M. Pijolat, M. Sennour, R. Molins, Oxidation kinetics and mechanisms of Ni-base alloys in pressurised water reactor primary conditions: influence of subsurface defects. Corros. Sci. **53**, 3914–3922 (2011)
25. S. Le Hong, C. Amzallag, A. Gelpi, Modelling the SCC initiation on alloy 600 in primary water of PWRs, in *9th International Conference on the Environmental Degradation of Materials in Nuclear Power Systems*, Newport Beach, CA, 1999